One-step fabrication of low resistance conductors on 3D printed structures by laser-induced graphene (LIG)

Mehraneh Tavakkoli Gilavan[1], Md Saifur Rahman[1,2], Aamir Minhas-Khan[1], Suresh Nambi[1],

Gerd Grau[1]*

[1] Department of Electrical Engineering and Computer Science, Lassonde School of Engineering, York University, 4700 Keele Street, Toronto, ON, M3J 1P3, Canada

[2] Thayer School of Engineering, Dartmouth College, 14 Engineering Drive, Hanover, NH, 03755, USA

*grau@eecs.yorku.ca

Abstract:

3D printing is becoming increasingly prevalent in manufacturing of goods for different applications. Many of these applications will benefit from the integration of electronics into 3D printed structures. In this study, we report a fabrication method to convert 3D printed polyetherimide (PEI) into graphene by exposing it to a scanned laser beam. This laser-induced graphene (LIG) is not only conductive, but also has a large gauge factor for mechanical strain sensing. We have achieved a sheet resistance of 0.30 Ω/sq which is 50 times lower than previous reports on 3D printed PEI/PC sheets and the lowest LIG sheet resistance value reported to date

1

on any polymer substrate. This is achieved due to three main factors: large thickness of LIG on a 3D printed object, maximization of the laser energy per unit area, and improved LIG morphology on 3D printed PEI compared with commercial PEI.

Keywords: Graphene, Laser induction, 3D print, Conductors, Low sheet resistance

1. Introduction

3D printing is a promising technology for additive manufacturing. Complex designs can be turned into solid parts layer by layer and can easily be customized[1]. Other advantages are minimum waste of materials and direct transformation to a finished product without subtractive methods or customized tooling such as dies or molds[2]. 3D printing has been employed in various industries such as aerospace, construction[3] or medical devices[4]. The integration of electronics into 3D printed structures would enable smart objects to be printed with additional functionality such as sensing, actuation or energy storage[5]. Multiple different carbon-based filaments have been explored for this application[6,7]. The combination of carbon nanotubes and thermoplastic polyurethane (CNT/TPU) is one of the most well-studied conductive 3D printing filaments. In one report, CNT/TPU filament was used to fabricate multiaxial force sensors, and the average conductivity of the filament was 7 S/m[8]. In another study, an extruded filament of CNT/TPU nanocomposite was created for fused deposition modeling (FDM) 3D printing. By loading 5 wt.% of CNT, the achieved conductivity was less than 10 S/m[9]. By using polybutylene terephthalate (PBT) with CNT, the obtained conductivity of the filament was around 20 S/m[7]. Also, graphene can be one of the promising candidates to fabricate 3D printed conductors. Graphene is exceptional due to its superior strength[10], high electrical conductivity[11], and high

2

thermal conductivity[12]. In addition, the large piezo-resistivity of graphene make it ideal for mechanical sensing applications. In one study, graphene/PBT filament was used to fabricate nanocomposites. The results showed a conductivity of 3 S/m for this filament[7]. In another report, the electrical conductivity of an acrylonitrile-butadiene-styrene (ABS) and graphene blend was investigated. By using different methods for blending, the best result for electrical conductivity was 7.29 S/m[13]. Further studies showed highly conductive graphene/poly-lactic acid (PLA) filament for flexible circuits fabrication with conductivity of 476 S/m[14]. Although this filament is highly conductive, the fabrication of graphene and also the filament itself is a complex process that leads to high cost[15]. Recently, a simple one-step laser-based process has been developed to fabricate conductors that transforms a polymer substrate into laser-induced graphene (LIG)[16]. LIG can be generated on polyimide (PI), polyetherimide (PEI), polyether ether ketone (PEEK), and other high temperature polymers by applying a CO_2 laser[17]. The graphene is easily patterned by scanning the laser beam. The properties of the graphene (conductivity and morphology) can be easily tuned for different applications by optimizing the laser conditions. Laser-induced graphene has been used as conductors in supercapacitors[18], electrochemical sensors[19], and water splitting[20].

Although there are several reports of laser-induced graphene on PI and other polymers, they all use flat substrates[21,22,23]. To the best of our knowledge, only one other recent study has reported LIG on a 3D printed substrate. In this work, a copolymer blend of PEI and polycarbonate (PC) (Ultem 9085) was used as the 3D printed substrate and the conductive layer was fabricated by CO_2 laser direct scanning in ambient air. The lowest obtained sheet resistance was 15.9 Ω/sq[24]. Here, we demonstrate laser-induced graphene on 3D printed PEI with 50 times lower sheet resistance, possibly because we did not use a copolymer and a smaller pulse spacing leading to a

larger laser energy per unit area. This opens up many applications to fabricate smart objects. Products can be 3D printed with conductive LIG directly integrated into or onto the structure (see illustration in Figure 1). PEI is particularly promising because it is an engineering plastic with superior mechanical properties. Additionally, 3D printed substrates have different physical properties compared with commercial sheets, which can affect the LIG process and the conductivity and morphology of the generated graphene, as demonstrated here for the first time. By optimizing the laser conditions, we have achieved very low sheet resistance compared to previous studies on flat PEI and 3D printed PEI/PC[17,24].

2. Experimental

The 3D printed substrates were designed using CAD software (Solidworks). Polyetherimide (ULTEM 1010) was used as the starting filament and 3D printed by fused deposition modeling (FDM) using a Stratasys Fortus 450mc printer. To engrave the 3D printed substrates, a CO_2 laser cutter (VersaLASER System (VLS2.30)) with 10.6 µm wavelength was used. The maximum laser power was 30 W and the average power was varied by pulse width modulation. The spacing between pulses was 1000 dots per inch (DPI), and the laser spot size was 76 µm. The laser scan rate was 2.54 cm/s in all the experiments. The effect of pattern size was studied with lines that were one, two or three pulses wide as well as rectangles that were 100 pulses wide (see Figure 1 (b) and (c) for an illustration of the laser process). The 3D printed substrate was compared to a commercial PEI sheet (ULT-0090-E) with the same thickness as the 3D printed substrate. The laser process was the same as for the 3D printed substrates using the rectangle pattern. The sheet resistance was measured using a four-point configuration, for rectangle patterns using a four-point probe resistivity measurement system (Signatone Pro4) and for line patterns using a probe station with a semiconductor parameter analyzer (Keithley 4200A).

Raman spectra were obtained with a Horiba Scientific (Model: LabRAM ARAMIS) Raman Microscope using 532 nm laser excitation with a laser power of 50 mW. To prepare samples for thickness measurement, they were coated with epoxy resin, then cured in room temperature for 24 hours, cut with a bandsaw and polished with sandpaper. The thickness of graphene layers was measured by optical microscopy. A field emission scanning electron microscope (FE-SEM) (Thermofisher Quanta 3D) was used to observe the morphology of engraved patterns. X-ray photoelectron spectroscopy (XPS) was performed using a K-alpha X-ray photoelectron spectrometer system. All of the survey spectra were recorded in 1 eV step size with a pass energy of 200 eV. Elemental spectra were recorded in 0.1 eV step sizes with a pass energy of 25 eV. Thermogravimetric analysis (TGA) (TGA55, TA Instruments) was carried out between 100 and 800°C at 10°C/min in air. A differential scanning calorimeter (DSC) (DSC250, TA Instruments) was used for the DSC analyses between 100 and 400°C at 10°C/min in air. The fabricated strain sensors were tested in a 3-point bending setup and a manual hydraulic press (10-Ton hydraulic press, MAXIMUM) was used to apply the strain. The samples were connected to a digital multimeter (Keithley 2110) to measure the resistance.

3. Results and Discussion

Figure 2 (a) shows sheet resistance for lines engraved with different power and width in terms of number of pulses. With increasing laser power, the sheet resistance for all line widths initially decreases. In the case of one pulse wide lines, by increasing power to 90% the lowest obtained sheet resistance is 6.39 Ω/sq. The lowest sheet resistance for two pulse wide lines is 2.56 Ω/sq. When the laser power is increased to more than 70%, the materials start to degrade and ablate. Three pulses wide lines exhibit a sheet resistance of 1.92 Ω/sq at 40% power, which is three times better than the lowest sheet resistance for one pulse wide lines. When the laser power is

increased to more than 40%, the materials start to degrade and ablate. Sheet resistance and the optimum power both decrease as the width of lines increases. The limiting case with a large width is a rectangle. As multiple lines are engraved, the thermal field of each line affects the adjacent lines, which improves the transformation to graphene. Therefore, the lowest obtained sheet resistance is 0.3 Ω/sq in a rectangle pattern. Similarly, smaller pulse spacing, i.e. larger DPI, improves pulse overlap and sheet resistance. Therefore, the largest DPI possible with this laser tool was used (DPI=1,000). For a better comparison between different parameters, energy per unit area is calculated for different patterns based on the following equations[25].

For a square or rectangle with a large width:

$$E_{AS} = \frac{xP}{v}N \tag{1}$$

For a finite width line that is n pulses wide:$E_{AL} = \frac{xPn}{v} / \left(w + \frac{n-1}{N}\right)$ (2)

Where x is percentage power (duty cycle), P is peak power in Watts, v is scan speed, N is resolution (the inverse of pulse spacing) in DPI converted to SI units, and w is the width of the laser beam.

Figure 2 (b) shows the calculated energy per unit area for one, two, and three pulse wide lines and rectangle patterns. To obtain 0.3 Ω/sq sheet resistance for a rectangle pattern, 1,850 J/cm^2 is needed. The LIG patterns on the 3D printed substrate are compared to the patterns on a commercial PEI sheet with the same thickness as the 3D printed sample to study the effect of the polymer. As shown in Figure 2 (c), the sheet resistance decreases for both polymers with increasing laser power up to 40%. By increasing the laser power to more than 40%, the polymers start to degrade. Although the decreasing trend in sheet resistance is similar for both polymers, the 3D printed substrate shows lower sheet resistance for the same laser power. The optimum

power is 40% for both 3D printed and commercial substrates. With the optimum power, the sheet resistance for the engraved pattern on the 3D printed substrate is 0.3 Ω/sq and for the commercial sample is 1.79 Ω/sq. The sheet resistance for the 3D printed substrate is 6 times lower than the commercial sample, which demonstrates the advantage of using 3D printed PEI.
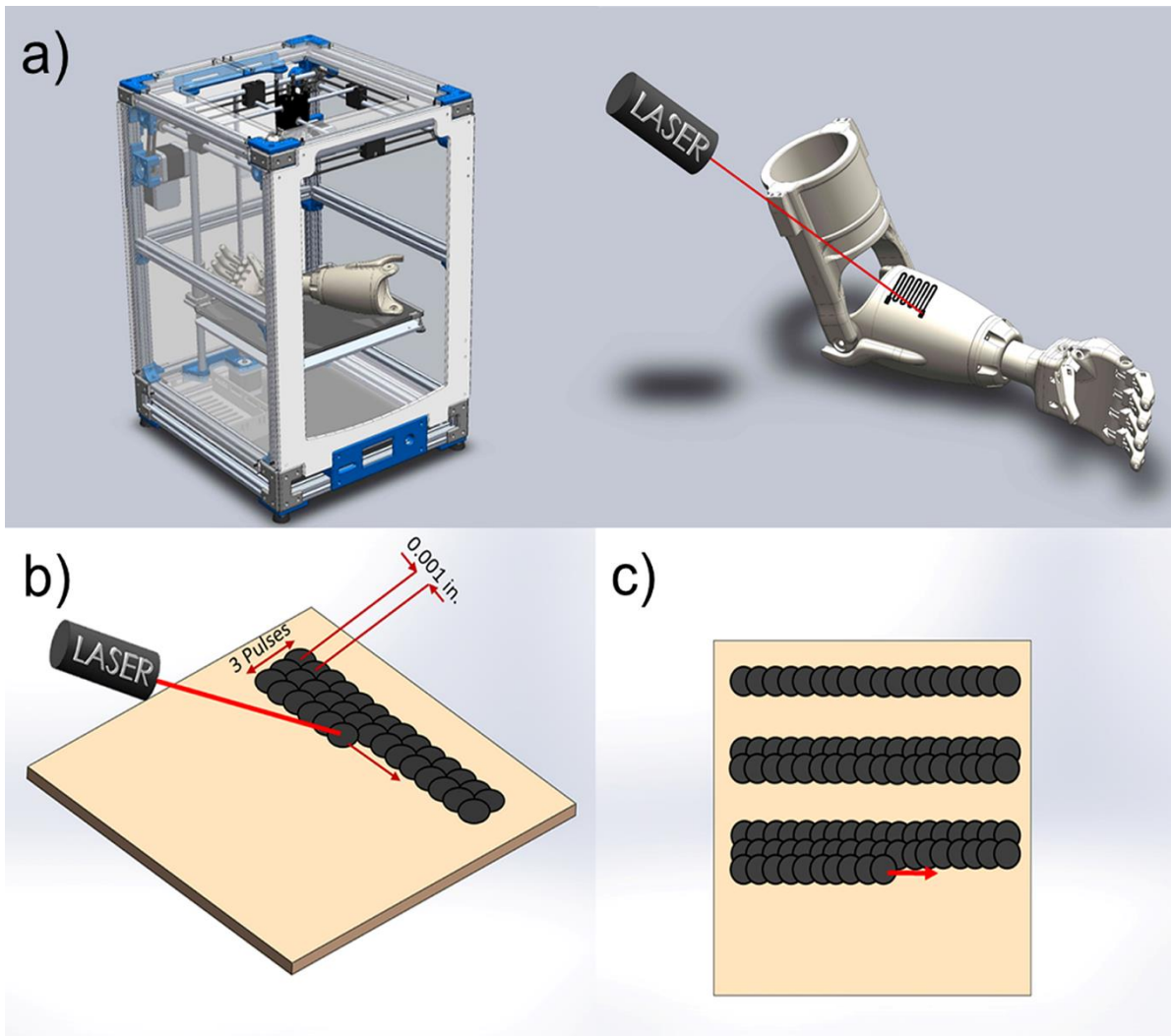

Figure 1. a) Schematic illustration of 3D printing the substrate and the laser process on the 3D printed object. The conductive patterns for different applications can be directly integrated into smart objects. b) Laser process on 3D printed PEI substrate. c) One, two, and three pulses wide lines on PEI substrates.
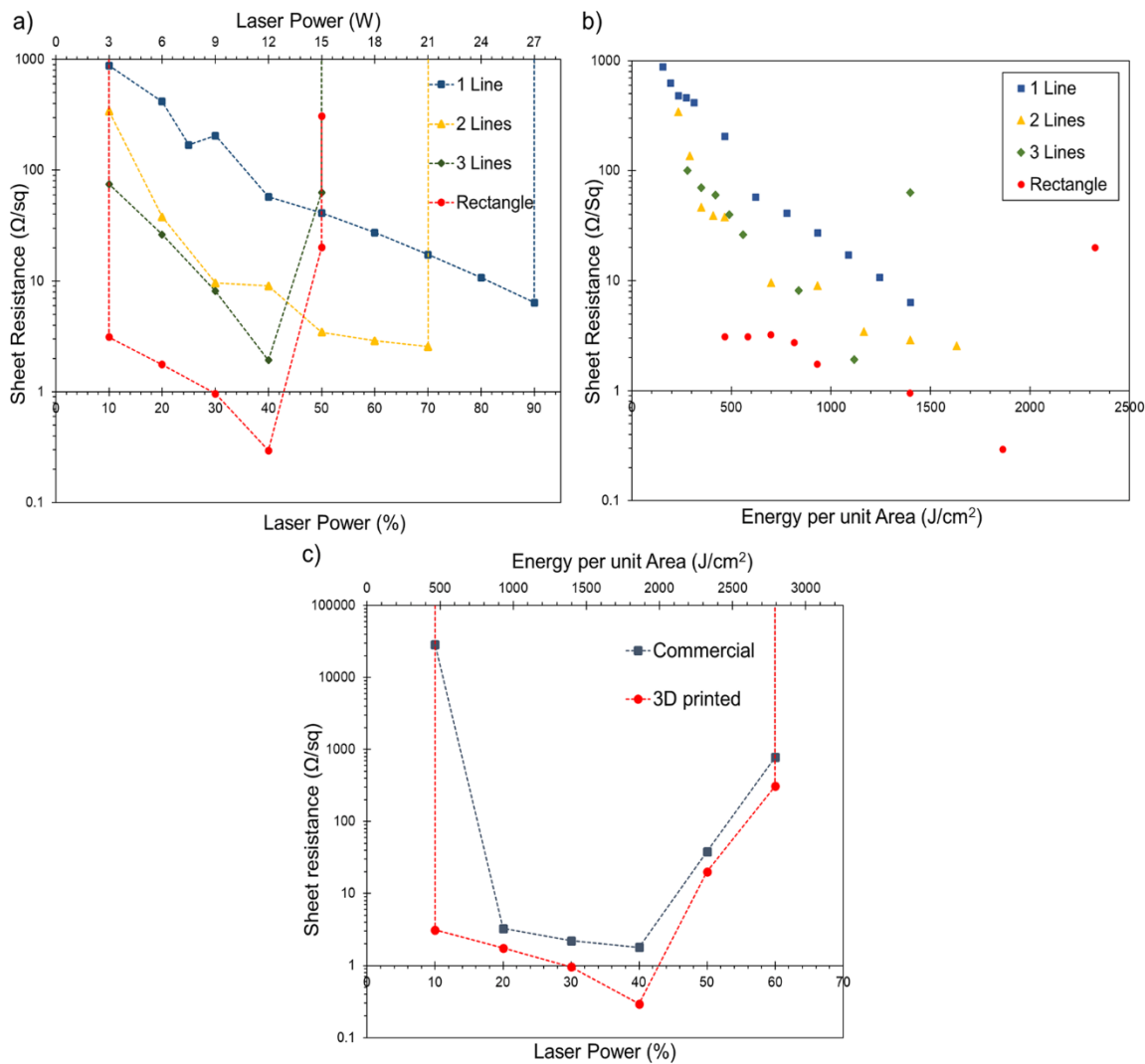
Figure 2. a) Sheet resistance measurements for 1, 2, 3 pulses wide lines, and rectangle patterns as a function of laser power. b) Sheet resistance as a function of calculated energy per unit area for different patterns. c) Effect of polymer on sheet resistance. Sheet resistance decreases with increasing power up to the where material is ablated and conductivity is lost (no data points on graph for large laser powers.) Sheet resistance decreases with increasing line width and is lower for 3D printed samples than commercial PEI sheets.

Figure 3 (a) to (h) show optical micrographs of the cross-section of three pulse wide lines with different laser powers on 3D printed and commercial samples. As shown in Figure 3 (a) and (b), at 10% power, the transformation only happens at the surface of the substrate. By increasing the power to 20%, the heat starts to diffuse inside the substrate and the graphene layer becomes thicker (Figure 3 (c) and (d)). At 40% power, the largest thickness is achieved (Figure 3 (g) and (h)). Engraved line width also increases with increasing laser power. The width of engraved lines on 3D printed PEI is wider compared to commercial samples. By comparing the 3D printed and commercial samples at each laser power, we can see the engraved lines are about 20% to 45% wider for 3D printed than commercial samples. Figure 3 (i) shows the correlation of resistivity and thickness with laser power for 3D printed and commercial samples. The thickness reported in Figure 3 (i) is the thickness at the thickest point of each line. Since the line cross-section is not rectangular, average thickness over the width of each line was used to calculate resistivity. Increasing laser power not only increases the graphene thickness but also improves material quality thereby decreasing resistivity. Large thickness and low resistivity combined result in low sheet resistance. The maximum thickness achieved here is approximately 600 µm. This is much thicker than conventional flexible polymer substrates, which means much lower sheet resistance can be obtained on thick 3D printed objects compared with LIG in flexible electronics systems.

The material quality was studied with Raman spectroscopy. Figure 4 (a) shows the Raman spectra for rectangle pattern samples with different laser powers on 3D printed substrates. All samples indicate D and G bands at 1300 cm^{-1} and 1550 cm^{-1}, respectively. However, for 10%, 20%, and 30% samples, the intensity of the peaks is not very high. Also, the D and G bands are connected corresponding to high-temperature annealed nano graphite[26]. At 40% power, a sharper 2D peak appears at 2690 cm^{-1} which signifies the presence of graphenic carbon[17]. Raman

spectroscopy results for commercial samples are shown in Figure 4 (b). For all the samples, G and D bands appear at around 1300 cm^{-1} and 1550 cm^{-1}. Same as for 3D printed samples, the D and G bands are not separated and form an interconnected peak that corresponds to high-temperature annealed nano graphite. The 2D peak in commercial samples is just a broad peak, and it is not as detectable as the 2D peak in the 40% power spectrum on the 3D printed substrate. The TEMs image in Figure 4 (c) and (d) confirm the formation of multilayer graphene flakes.

3D Printed   Commercial

a) b) c) d) e) f) g) h)

120 µm

i)

Laser Power (W)

Commercial
3D printed

Resistivity (Ω.m)
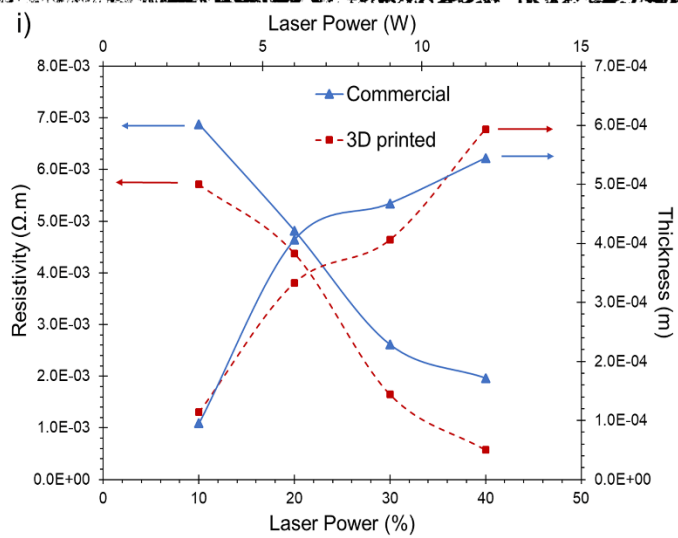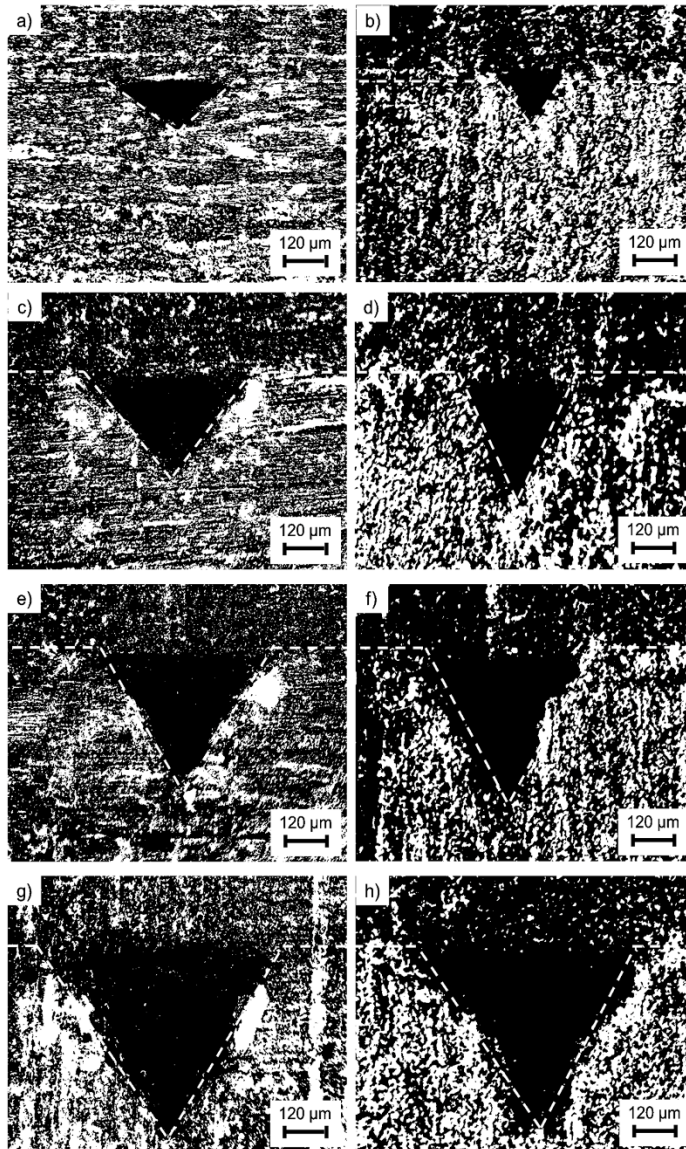Thickness (m)
Laser Power (%)

11

Figure 3. Cross-sectional optical micrographs of three pulse wide lines on 3D printed and commercial substrates for a,b) 10%, c,d) 20%, e,f) 30%, g,h) 40% laser power, respectively. Line width and depth increase with increasing laser power. The increase in the line width is clearer in 3D printed samples compared to commercial samples. i) Resistivity and thickness as a function of laser power for three pulse wide lines in 3D printed and commercial samples. Reported thickness is the for the thickest part of the line and average thickness is used in resistivity calculation. The increase in thickness and decrease in resistivity with increasing power combine to achieve a low sheet resistance.
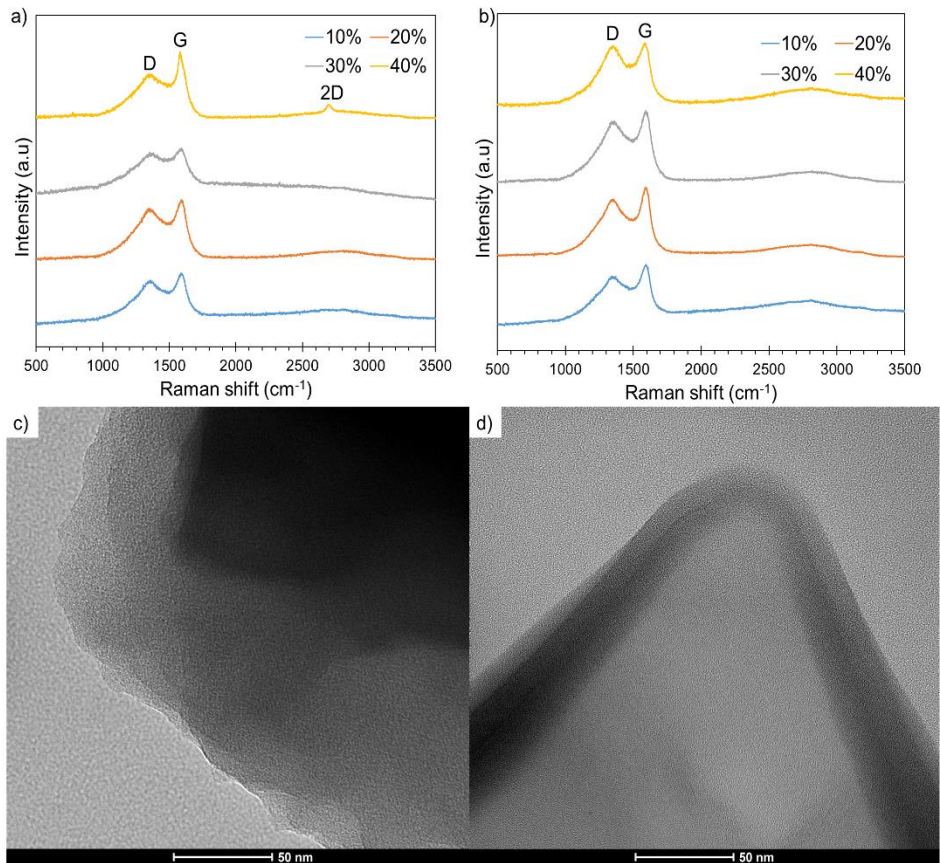

Figure 4. Raman spectra for rectangle patterns with different laser powers on a) 3D printed PEI and b) commercial PEI. Material quality improves with power. Multilayer graphene peaks can be observed at 40% power for the 3D printed PEI. TEM images for 40% laser power on c) 3D printed PEI and d) commercial PEI.

Figure 5 shows the morphology of both 3D printed and commercial PEI for different laser powers at lower magnification. For 10% power, the laser passes are differentiable on both substrates (Figure 5 (a) and (b)). By increasing the power to 20%, the laser passes in the 3D printed sample are more disordered, but they are still distinguishable. Unlike on the 3D printed sample, the surface morphology of the commercial sample is changed, and laser passes are not detectable. Higher powers change the surface morphology of commercial samples completely, and the features have irregular shapes (Figure 5 (f) and (h)). The features grow significantly, and large-scale porosity is more pronounced for the commercial samples, which may explain the higher resistivity. The inset images show the formation of microscale dendritic defects on the surface of the 3D printed samples. As indicated in the images, the size of defects changes with changing laser power. The biggest size defect is observed for 20% power. Also, the planar defect density for this sample is 8.5 /mm^2 which is the highest among the studied samples. The defect density for 40% power is 3.6 /mm^2 and the size of these defects is much smaller than for the other samples. At high power, there is more energy for the transformation of PEI to graphene and less time for defect growth, which explains the improvement in electrical conductivity. There is no indication of microscale dendritic defects on the surface of commercial samples. High-resolution SEM images for both 3D printed and commercial samples are shown in Figure S1 and S2 (Supporting Information). There are no significant differences between 3D printed and commercial PEI samples. When laser power is low, the LIG is made up of intertwined branches with low porosity. By increasing the laser power, the branches start to grow, and the porosity is increased.
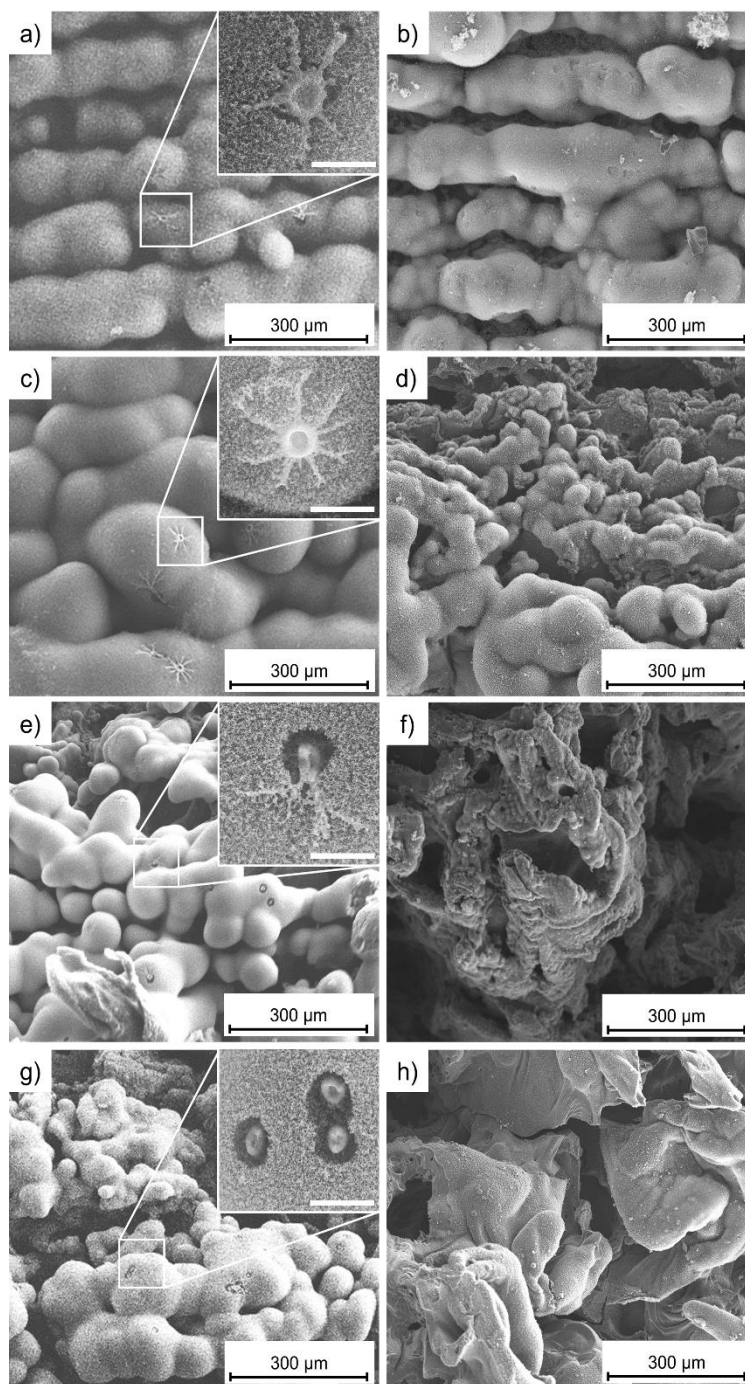
Figure 5. Low-magnification SEM images of the graphene surface in rectangle pattern samples at a) 10%, c) 20%, e) 30%, g) 40% laser power on 3D printed PEI substrate. SEM images of the graphene surface in rectangle pattern samples at b) 10%, d) 20%, f) 30%, h) 40% laser power on commercial PEI substrate. The inset images show the formation of microscale dendritic defects on the surfaces of 3D printed samples. (Inset scale bar: 20 µm).

Figure 6 (a) shows the DSC thermograms for 3D printed and commercial PEI samples. Both samples exhibit a similar transition corresponding to the glass transition at 221°C. The DSC results show the enthalpy for 3D printed PEI is different from commercial PEI. The specific enthalpy for the 3D printed sample is 3.11 J/g, and for the commercial sample is 0.95 J/g. Heating polymers such as PEI (e.g. during 3D printing) can lead to the appearance of sharp endothermic peaks at the glass transition. This endothermic peak is associated with enthalpy relaxation due to physical aging after heating the samples[27]. During the 3D printing process, the filament is heated, and chains rearrange themselves into a close-packed configuration. Therefore, the physical aging appears in 3D printed samples, and the endothermic peak is significant. It can be concluded that 3D printing changes the properties of the PEI. These differences between 3D printed and commercial PEI may lead to different interactions with the laser and formation of the graphene. Figure 6 (b) shows the thermogravimetric (TG) curves and their derivative (DTG) for 3D printed and commercial PEI. Both samples show good thermal stability up to about 450°C under air atmosphere. The mass change thereafter is due to main-chain scission and the release of volatile products. The mass loss in 3D printed PEI is 3.5% more than the commercial sample. Since the chemical composition of 3D printed and commercial PEI is similar, this difference in mass loss can again be due to physical aging in 3D printed samples.
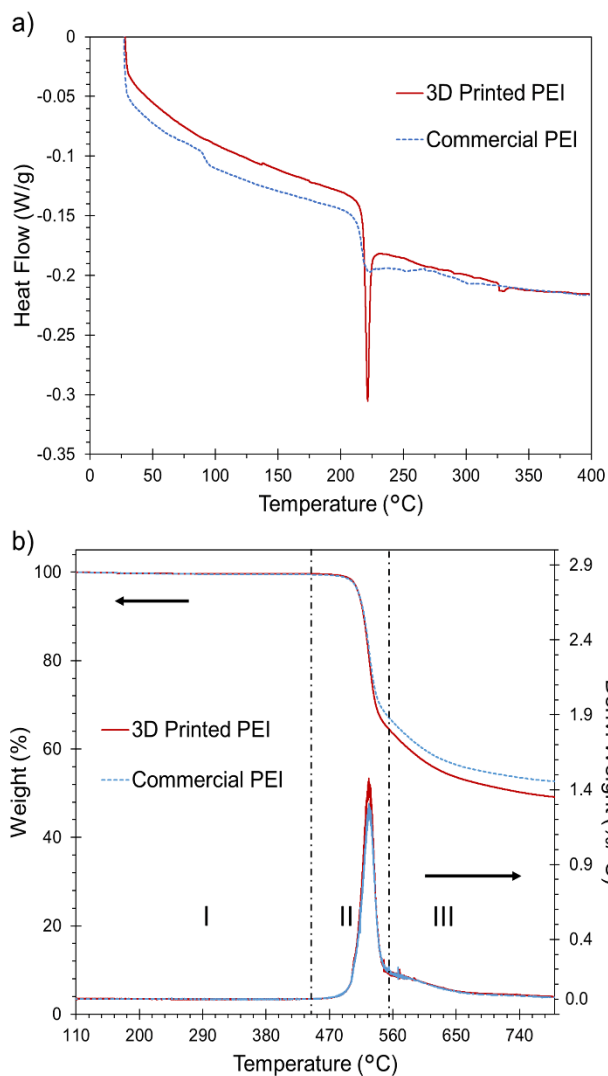
Figure 6. a) DSC thermograms of 3D printed and commercial PEI. The sharp endothermic peak at the glass transition is due to the physical aging of PEI during 3D printing. b) TG and DTG analysis of 3D printed and commercial PEI. The mass loss in 3D printed PEI is 3.5% more than in the commercial sample.

X-ray photoelectron spectroscopy is utilized to study the chemical nature of samples on 3D printed and commercial PEI. Figure 7 shows the XPS survey spectra and atomic percentages of carbon and oxygen in each sample. The curves in Figure 7 show that 3D printed and commercial PEI have approximately the same chemical composition. This means that the different LIG outcomes are due to physical differences between the commercial and 3D printed PEI as

16

characterized by TGA and DSC. After the laser process, the intensity of oxygen peaks is reduced to a great extent for both substrates. The atomic percentage of carbon is 65% before LIG conversion, and it increases to more than 80% in all samples. The atomic percentage of oxygen is reduced to less than 10% for commercial samples and 13% for the 3D printed samples. Although the lowest sheet resistance is achieved with 40% power in both 3D printed and commercial samples, the atomic percentage of carbon is not the maximum value in these samples. As the power approaches the ablation threshold, the LIG starts to oxidize resulting in an increase in the oxygen percentage. The lowest sheet resistance in these samples is not only a function of carbon percentage but also of morphology and thickness. Figure S3 and S4 (Supporting Information) show the deconvolution of C1s and O1s peaks for LIG samples as well as the 3D printed and commercial PEI substrates. These results show a decrease in sp^3 carbon and an increase in sp^2 carbon after the transformation from both PEI substrates to LIG. In the LIG samples, one can also observe the presence of a π-π* shake-up satellite. This provides further indication of high degree of graphenization[28].
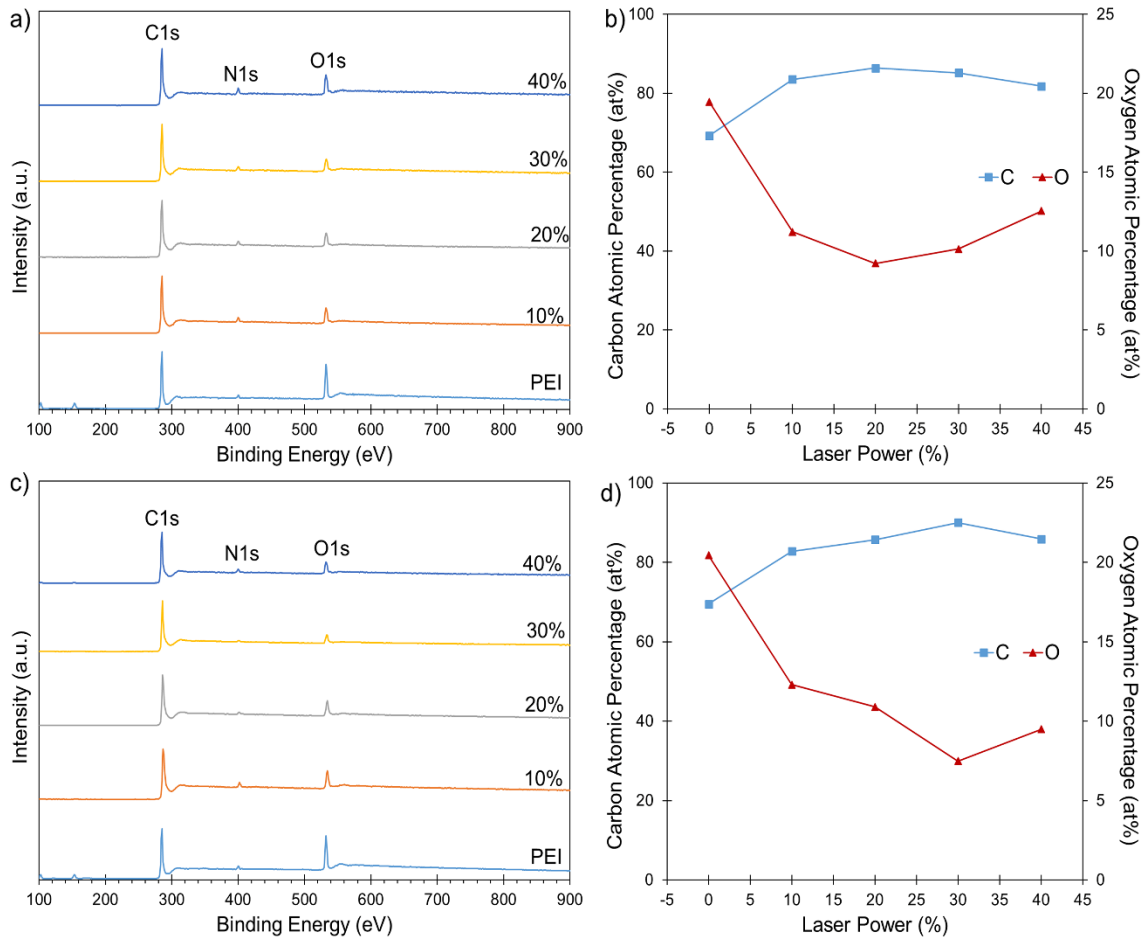
Figure 7. a) XPS survey spectra and b) atomic percentages of carbon and oxygen as a function of laser power for rectangle-patterned LIG on 3D printed PEI. c) XPS survey spectra and d) atomic percentages of carbon and oxygen as a function of laser power for LIG samples on commercial PEI.

To test the fabricated conductors in an application, a strain gauge is engraved on both 3D printed and commercial substrates. Figure 8 (a) shows the fabricated strain gauge on each substrate. The initial resistance of the strain gauge on the 3D printed PEI is 1.1 kΩ and for the strain gauge on the commercial PEI it is 1.5 kΩ. Figure 8 (b) shows a photograph of the 3-point bending setup used to test the fabricated strain sensors in tension mode. The engraved connection pads on each sample are connected to a digital multimeter to measure the resistance as a function of applied strain. As shown in Figure 8 (c) and (d), there are two different regions in each sample with a low gauge factor for small strain and a higher gauge factor for larger strain. Similar behavior has

been observed before in LIG strain sensors on flexible substrates[29,30]. In the 3D printed sample, up to 0.9% strain, the change in resistance is small and the gauge factor is around 11. By increasing the applied strain up to 1.5%, the gauge factor increases to 100. Even though the initial resistance for both samples is close, the behavior of the commercial sample is very different in the bending test. The gauge factor for applied strain below 0.3% is 2.5. The difference between 3D printed and the commercial sample is more significant in the second region, and gauge factor is around 14 times larger for the 3D printed sample. Based on the mechanical measurement, the fabricated conductors on 3D printed PEI show better piezoresistivity and are a better option for strain sensors. By integrating LIG conductors into 3D printed structures, we can take advantage of complicated designs along with low sheet resistance and high gauge factor.
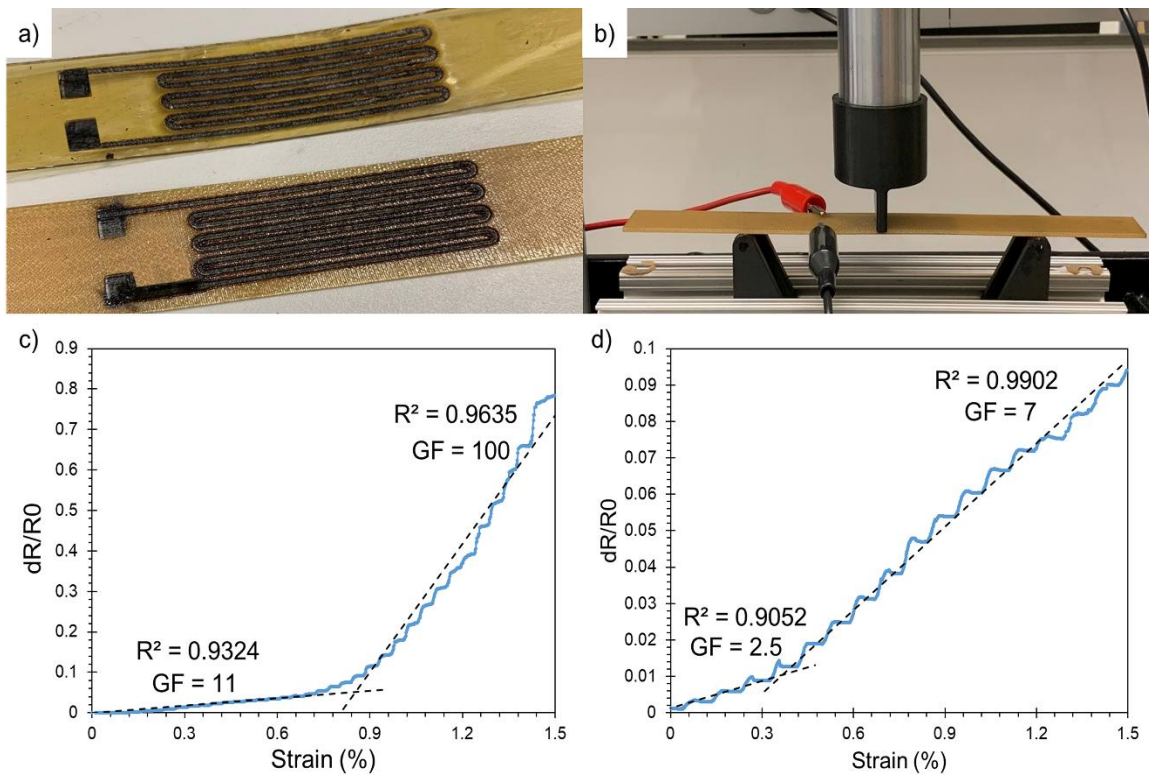

Figure 8. a) Strain gauge engraved on 3D printed (bottom) and commercial (top) PEI. b) The three-point bending test setup. Resistance change after applying strain to the engraved strain gauge on c) 3D printed PEI and d) commercial PEI.

19

4. Conclusions

We have demonstrated the direct conversion of a 3D printed polymer (PEI) into graphene by using a CO_2 laser. Sheet resistance was optimized by varying the laser power and pattern. Increasing power and line width reduces sheet resistance and defect density up to the point where material is ablated. 40% laser power gave the best result. Much lower sheet resistance (0.30 Ω/sq) was achieved on the 3D printed PEI compared with commercial sheets as well as previous reports on 3D printed PEI/PC and on other substrates. Although both samples had similar chemical compositions, the morphology of LIG on 3D printed samples was very different. Due to the rearrangement of chains during the 3D printing process, the thermal analysis of the 3D printed PEI showed different results. Strain sensors fabricated on 3D printed PEI showed 14 times higher gauge factor compared to commercial samples. This technique enables the facile integration of electronics on different 3D printed geometries and structures opening up many different applications for 3D printed smart objects.

Supporting Information

SEM images of the graphene surface on rectangle pattern samples for 3D printed and commercial PEI; deconvoluted XPS spectra of O1s and C1s peaks of 40% laser power LIG on 3D printed and commercial PEI samples and substrates.

Acknowledgments

References

(1)   Ngo, T. D.; Kashani, A.; Imbalzano, G.; Nguyen, K. T. Q.; Hui, D. Additive Manufacturing (3D Printing): A Review of Materials, Methods, Applications and Challenges. *Compos. Part B Eng.* **2018**, *143* (December 2017), 172–196. https://doi.org/10.1016/j.compositesb.2018.02.012.

(2)   Huang, S. H.; Liu, P.; Mokasdar, A.; Hou, L. Additive Manufacturing and Its Societal Impact: A Literature Review. *Int. J. Adv. Manuf. Technol.* **2013**, *67* (5–8), 1191–1203. https://doi.org/10.1007/s00170-012-4558-5.

(3)   Tay, Y. W. D.; Panda, B.; Paul, S. C.; Noor Mohamed, N. A.; Tan, M. J.; Leong, K. F. 3D Printing Trends in Building and Construction Industry: A Review. *Virtual Phys. Prototyp.* **2017**, *12* (3), 261–276. https://doi.org/10.1080/17452759.2017.1326724.

(4)   Ho, C. M. B.; Ng, S. H.; Yoon, Y. J. A Review on 3D Printed Bioimplants. *Int. J. Precis. Eng. Manuf.* **2015**, *16* (5), 1035–1046. https://doi.org/10.1007/s12541-015-0134-x.

(5)   Perez, K. B.; Williams, C. B. Combining Additive Manufacturing and Direct Write for Integrated Electronics - A Review. *24th Int. SFF Symp. - An Addit. Manuf. Conf. SFF 2013* **2013**, 962–979.

(6)   Kwok, S. W.; Goh, K. H. H.; Tan, Z. D.; Tan, S. T. M.; Tjiu, W. W.; Soh, J. Y.; Ng, Z. J. G.; Chan, Y. Z.; Hui, H. K.; Goh, K. E. J. Electrically Conductive Filament for 3D-Printed Circuits and Sensors. *Appl. Mater. Today* **2017**, *9*, 167–175.

https://doi.org/10.1016/j.apmt.2017.07.001.

(7)   Gnanasekaran, K.; Heijmans, T.; van Bennekom, S.; Woldhuis, H.; Wijnia, S.; de With, G.; Friedrich, H. 3D Printing of CNT- and Graphene-Based Conductive Polymer Nanocomposites by Fused Deposition Modeling. *Appl. Mater. Today* **2017**, *9*, 21–28. https://doi.org/10.1016/j.apmt.2017.04.003.

(8)   Kim, K.; Park, J.; Suh, J. hoon; Kim, M.; Jeong, Y.; Park, I. 3D Printing of Multiaxial Force Sensors Using Carbon Nanotube (CNT)/Thermoplastic Polyurethane (TPU) Filaments. *Sensors Actuators, A Phys.* **2017**, *263*, 493–500. https://doi.org/10.1016/j.sna.2017.07.020.

(9)   Christ, J. F.; Aliheidari, N.; Ameli, A.; Pötschke, P. 3D Printed Highly Elastic Strain Sensors of Multiwalled Carbon Nanotube/Thermoplastic Polyurethane Nanocomposites. *Mater. Des.* **2017**, *131*, 394–401. https://doi.org/10.1016/j.matdes.2017.06.011.

(10)   Ovid'ko, I. A. Mechanical Properties of Graphene. *Rev. Adv. Mater. Sci.* **2013**, *34* (1), 1–11.

(11)   Wang, J.; Ma, F.; Liang, W.; Sun, M. Electrical Properties and Applications of Graphene, Hexagonal Boron Nitride (h-BN), and Graphene/h-BN Heterostructures. *Mater. Today Phys.* **2017**, *2*, 6–34. https://doi.org/10.1016/j.mtphys.2017.07.001.

(12)   Pop, E.; Varshney, V.; Roy, A. K. Thermal Properties of Graphene: Fundamentals and Applications. *MRS Bull.* **2012**, *37* (12), 1273–1281. https://doi.org/10.1557/mrs.2012.203.

(13)   Singh, R.; Sandhu, G. S.; Penna, R.; Farina, I. Investigations for Thermal and Electrical Conductivity of ABS-Graphene Blended Prototypes. *Materials (Basel).* **2017**, *10* (8). https://doi.org/10.3390/ma10080881.

(14)   Zhang, D.; Chi, B.; Li, B.; Gao, Z.; Du, Y.; Guo, J.; Wei, J. Fabrication of Highly Conductive Graphene Flexible Circuits by 3D Printing. *Synth. Met.* **2016**, *217*, 79–86. https://doi.org/10.1016/j.synthmet.2016.03.014.

(15)   Huang, X.; Yin, Z.; Wu, S.; Qi, X.; He, Q.; Zhang, Q.; Yan, Q.; Boey, F.; Zhang, H. Graphene-Based Materials: Synthesis, Characterization, Properties, and Applications. *Small* **2011**, *7* (14), 1876–1902. https://doi.org/10.1002/smll.201002009.

(16)   Lin, J.; Peng, Z.; Liu, Y.; Ruiz-Zepeda, F.; Ye, R.; Samuel, E. L. G.; Yacaman, M. J.; Yakobson, B. I.; Tour, J. M. Laser-Induced Porous Graphene Films from Commercial Polymers. *Nat. Commun.* **2014**, *5*, 1–8. https://doi.org/10.1038/ncomms6714.

(17)   Chyan, Y.; Ye, R.; Li, Y.; Singh, S. P.; Arnusch, C. J.; Tour, J. M. Laser-Induced Graphene by Multiple Lasing: Toward Electronics on Cloth, Paper, and Food. *ACS Nano* **2018**, *12* (3), 2176–2183. https://doi.org/10.1021/acsnano.7b08539.

(18)   Peng, Z.; Lin, J.; Ye, R.; Samuel, E. L. G.; Tour, J. M. Flexible and Stackable Laser-Induced Graphene Supercapacitors. *ACS Appl. Mater. Interfaces* **2015**, *7* (5), 3414–3419. https://doi.org/10.1021/am509065d.

(19)   Nayak, P.; Kurra, N.; Xia, C.; Alshareef, H. N. Highly Efficient Laser Scribed Graphene Electrodes for On-Chip Electrochemical Sensing Applications. *Adv. Electron. Mater.*

2016, *2* (10), 1–11. https://doi.org/10.1002/aelm.201600185.

(20) Ye, R.; Chyan, Y.; Zhang, J.; Li, Y.; Han, X.; Kittrell, C.; Tour, J. M. Laser-Induced Graphene Formation on Wood. *Adv. Mater.* **2017**, *29* (37), 1–7. https://doi.org/10.1002/adma.201702211.

(21) Ye, R.; James, D. K.; Tour, J. M. Laser-Induced Graphene: From Discovery to Translation. *Adv. Mater.* **2019**, *31* (1), 1–15. https://doi.org/10.1002/adma.201803621.

(22) Wang, F.; Wang, K.; Zheng, B.; Dong, X.; Mei, X.; Lv, J.; Duan, W.; Wang, W. Laser-Induced Graphene: Preparation, Functionalization and Applications. *Mater. Technol.* **2018**, *33* (5), 340–356. https://doi.org/10.1080/10667857.2018.1447265.

(23) Li, Y.; Luong, D. X.; Zhang, J.; Tarkunde, Y. R.; Kittrell, C.; Sargunaraj, F.; Ji, Y.; Arnusch, C. J.; Tour, J. M. Laser-Induced Graphene in Controlled Atmospheres: From Superhydrophilic to Superhydrophobic Surfaces. *Adv. Mater.* **2017**, *29* (27), 1–8. https://doi.org/10.1002/adma.201700496.

(24) Jiao, L.; Chua, Z. Y.; Moon, S. K.; Song, J.; Bi, G.; Zheng, H.; Lee, B.; Koo, J. Laser-Induced Graphene on Additive Manufacturing Parts. *Nanomaterials* **2019**, *9* (1), 1–9. https://doi.org/10.3390/nano9010090.

(25) Minhas-Khan, A.; Nambi, S.; Grau, G. Low-Resistance Laser-Induced Graphitic Carbon by Maximizing Energy Delivery and Pulse Overlap. *Carbon N. Y.* **2021**, *181*, 310–322. https://doi.org/10.1016/j.carbon.2021.05.037.

(26) Chu, P. K.; Li, L. Characterization of Amorphous and Nanocrystalline Carbon Films. *Mater. Chem. Phys.* **2006**, *96* (2–3), 253–277. https://doi.org/10.1016/j.matchemphys.2005.07.048.

(27) Mzabi, N.; Smaoui, H.; Guermazi, H.; Mlik, Y.; Agnel, S.; Toureille, A. Heating Effects on Structural and Electrical Properties of Polyetherimide. *Am. J. Eng. Appl. Sci.* **2009**, *2* (1), 120–126. https://doi.org/10.3844/ajeassp.2009.120.126.

(28) Lamberti, A.; Perrucci, F.; Caprioli, M.; Serrapede, M.; Fontana, M.; Bianco, S.; Ferrero, S.; Tresso, E. New Insights on Laser-Induced Graphene Electrodes for Flexible Supercapacitors: Tunable Morphology and Physical Properties. *Nanotechnology* **2017**, *28* (17). https://doi.org/10.1088/1361-6528/aa6615.

(29) Liu, W.; Huang, Y.; Peng, Y.; Walczak, M.; Wang, D.; Chen, Q.; Liu, Z.; Li, L. Stable Wearable Strain Sensors on Textiles by Direct Laser Writing of Graphene. *ACS Appl. Nano Mater.* **2020**, *3* (1), 283–293. https://doi.org/10.1021/acsanm.9b01937.

(30) Rahimi, R.; Ochoa, M.; Yu, W.; Ziaie, B. Highly Stretchable and Sensitive Unidirectional Strain Sensor via Laser Carbonization. *ACS Appl. Mater. Interfaces* **2015**, *7* (8), 4463–4470. https://doi.org/10.1021/am509087u.